Silva, G. T., Tian, L., Franklin, A., Wang, X., Han, X., Mann, S., & Drinkwater, B. W. (2019). Acoustic deformation for the extraction of mechanical properties of lipid vesicle populations. *Physical Review E*, *99*(6), [063002]. https://doi.org/10.1103/PhysRevE.99.063002

# Acoustic deformation for the extraction of mechanical properties of lipid vesicle populations

Glauber T. Silva,[1,*] Liangfei Tian,[2,†] Amanda Franklin,[3] Xuejing Wang,[4] Xiaojun Han,[4] Stephen Mann,[2,‡] and Bruce W. Drinkwater[3,§]

[1]*Physical Acoustics Group, Instituto de Física, Universidade Federal de Alagoas, Maceió, AL 57072-970, Brazil*

[2]*Centre for Protolife Research and Centre for Organized Matter Chemistry, School of Chemistry, University of Bristol, Bristol BS8 1TS, United Kingdom*

[3]*Department of Mechanical Engineering, University of Bristol, Bristol BS8 1TR, United Kingdom*

[4]*State Key Laboratory of Urban Water Resource and Environment, School of Chemistry and Chemical Engineering, Harbin Institute of Technology, Harbin, Heilongjiang 150001, China*

(Received 5 February 2019; revised manuscript received 11 April 2019; published 24 June 2019)

We use an ultrasonic standing wave to simultaneously trap and deform thousands of soft lipid vesicles immersed in a liquid solution. In our device, acoustic radiation stresses comparable in magnitude to those generated in optical stretching devices are achieved over a spatial extent of more than ten acoustic wavelengths. We solve the acoustic scattering problem in the long-wavelength limit to obtain the radiation stress. The result is then combined with thin-shell elasticity theory to form expressions that relate the deformed geometry to the applied acoustic field intensity. Using observation of the deformed geometry and this model, we rapidly extract mechanical properties, such as the membrane Young's modulus, from populations of lipid vesicles.

DOI: 10.1103/PhysRevE.99.063002

## I. INTRODUCTION

Measurement of the mechanical properties of biological cells, also known as mechanophenotyping, is becoming an indispensable tool in biophysics. These properties, also known as mechanical biomarkers, relate to the deformability or the resistance to deformation of a cell in response to applied stresses. Recent findings have shown that mechanophenotyping of cells can be used to analyze their state, function, and to track changes during biological processes such as stem cell differentiation [1], leukocyte activation [2], changes in red blood cells when infected with *Plasmodium faciparum* (malaria) [3], and cancer metastasis [4]. Different techniques have been proposed to examine cell deformation under external stresses, for example, micropipette aspiration [5], optical stretching [6], and atomic force microscopy [7]. Advances in laboratory-on-a-chip technology have also allowed the development of microfluidic-based methods that use flow-induced stresses for mechanophenotyping with high throughput, e.g., deforming thousands of single cells within minutes [8,9].

The nonlinear interaction of ultrasonic waves with an object gives rise to time-averaged acoustic radiation stresses. The overall contribution of these stresses on the object surface is termed the acoustic radiation force [10–12]. This force has been applied in laboratory-on-a-chip technology for trapping, sorting, and neatly positioning biological and chemical specimens (cells, microorganisms, and colloids) in the micrometer range [13–17].

Typically, an acoustic standing wave is employed to trap or focus microparticles in pressure nodes (zero pressure) and antinodes (maximum pressure). When a lipid vesicle (microvesicle) is trapped by the acoustic radiation force, the resulting stresses can also deform its geometry. The deformation induced by acoustic radiation stresses was first observed in hydrocarbon droplets in water with a diameter in the range of 0.2–2 mm [18,19]. More recently, it was demonstrated that swollen red blood cells (sRBCs), which have a spherical shape, can be deformed in a resonant microfluidic channel [20]. A green algae cell was also acoustically deformed in a half-wavelength microfluidic channel [21]. In both these works, the Young's modulus of each cell membrane was estimated through an iterative algorithm. In a different approach, a highly focused ultrasonic beam was employed to deform breast cancer cells [22]. This method showed that highly invasive cancer cells exhibited greater deformability than weakly invasive ones.

Here we demonstrate the use of an ultrasonic standing wave device of many wavelengths in size for acoustic deformation which has the potential to trap and deform thousands of cells simultaneously. In this way, the mechanical properties of populations of microparticles can be extracted, in a timescale of a few minutes. In a set of experiments, we analyzed the acoustic deformation of soft lipid-membraned particles called giant unilamellar vesicles (GUVs) which were prepared from 1,2-dioleoyl-*sn*-glycero-3-phosphocholine (DOPC) of which membrane is in the disordered liquid crystalline state at room temperature. We chose GUVs because they have a simple structure making them ideal for studying biomembrane mechanics [23–26]. Also, GUVs mimic cell membranes for both physical and biological investigations. We thus present an analytical model for acoustic deformation of soft spherical

*gtomaz@fis.ufal.br
†liangfei.tian@bristol.ac.uk
‡s.mann@bristol.ac.uk
§b.drinkwater@bristol.ac.uk

 

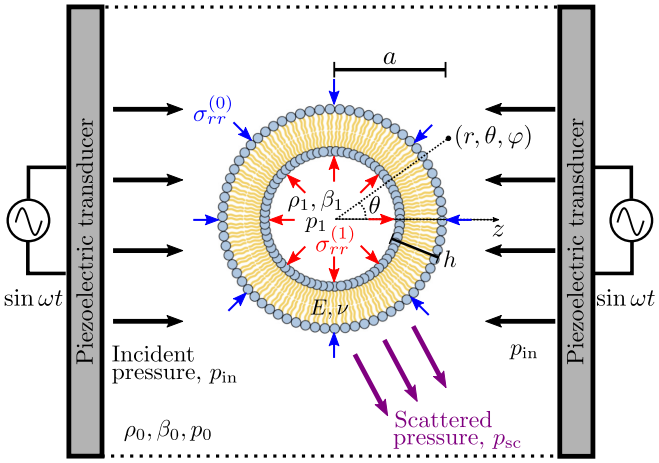


FIG. 1. Acoustic deformation device: two opposite piezoelectric transducers driven with a sinusoidal signal of frequency $\omega$ produce a standing wave (dark arrows) on a microvesicle immersed in a solution with pressure $p_{in}$. A microvesicle of radius $a$ has a membrane of thickness $h$ which encompasses a liquid core of density $\rho_1$, compressibility $\beta_1$, and ambient pressure $p_1$. The membrane is considered to be an isotropic elastic solid with Young's modulus $E$ and Poisson's ratio $\nu$. The surrounding liquid has density $\rho_0$, compressibility $\beta_0$, and ambient pressure $p_0$. The scattered pressure $p_{sc}$ is depicted by magenta arrows. The outer and inner acoustic radiation stresses are denoted by $\sigma_{rr}^{(0)}$ and $\sigma_{rr}^{(1)}$, respectively. Note device and particle are not to scale.

microvesicles immersed in a liquid caused by an ultrasonic standing wave. The experimental deformation results are in good qualitative and quantitative agreement with our theoretical predictions.

## II. ACOUSTIC DEFORMATION METHOD

Figure 1 shows a schematic of the acoustic deformation device which consists of two piezoelectric transducers arranged as the sides of a rectangular chamber of dimensions 20 mm × 20 mm × 2 mm. The piezoeletric transducers (15 mm × 2 mm × 1 mm) operate at 6.70 MHz with a corresponding wavelength $\lambda = 220\ \mu$m; hence the device chamber measures $67\lambda \times 67\lambda$. The piezoelectric transducers are excited with a sinusoidal voltage of the appropriate frequency and a peak-to-peak amplitude between 1 and 10 $V_{pp}$. An inverted microscope (Leica DMI3000 B, Wetzlar, Germany) was used for fluorescent imaging of the microvesicles in the device's central area (working area of 1 mm × 1 mm). Hence the device is simple to fabricate with low-cost components.

The device's chamber is filled with a liquid with density $\rho_0$, compressibility $\beta_0$, and speed of sound $c_0$. The transducers are wired in parallel and driven by a sinusoidal voltage of angular frequency $\omega$ to produce a one-dimensional standing wave in the chamber. The GUVs are injected into the chamber. They have a lipid bilayer membrane of thickness $h$ that encloses a liquid core of compressibility $\beta_1$, density $\rho_1$, and speed of sound $c_1$. Typically, the GUV diameter ranges from 1 to 100 $\mu$m, while its membrane thickness is a few nanometers [27]. Hence we assume $h \ll a$. The membrane is assumed to be an isotropic elastic solid according to Hooke's law and described by a Young's modulus $E$ and Poisson's ratio $\nu$. The internal fluid is assumed to be incompressible.

Figure 2 illustrates typical experimental results in which acoustic deformation of GUVs is performed in a glucose aqueous solution (see Supplemental Material [28]). Figures 2(a) and 2(b) show that about 100 GUVs can be trapped in a 1 mm × 1 mm region. We note that the number of trapped microparticles in a single experiment can reach thousands by using a microscope with a wider field of view. Details on the materials and methods are presented in the Supplemental Material [28].

The protocol to acoustically deform the GUVs is as follows. The prepared aqueous solution containing GUVs was injected into the device's chamber. After waiting a few minutes, the GUVs are sedimented to the bottom of the chamber. The transducers are excited with a voltage of 8 $V_{pp}$ in order to prealign the GUVs at the pressure nodes. The transducers were then switched off, and Fig. 2(a) shows a representative image of the prealigned GUVs array from which the radius of each individual GUV is measured. To avoid the influence of short-range stresses (contact, electrostatic, and van der Waals forces) in the measurements, we consider only isolated GUVs many micrometers apart. The transducers are then turned on for 1 min to avoid the initial transient period, and then an image is taken of the central area of the acoustic trapping chamber (1 mm × 1 mm or $4.5\lambda \times 4.5\lambda$) at different excitation voltages (8–10 $V_{pp}$), leading to the observed deformation of the GUV population [Fig. 2(b)]. We noted that the steady-state deformation is achieved in a few seconds as shown in the Supplemental Material Fig. S2 [28]. Moreover, a real-time GUV deformation is illustrated in the Supplemental Material Movie S1 [28]. The deformation of an isolated GUV of radius $a = 15.5\ \mu\text{m} = 0.07\lambda$ is illustrated in Figs. 2(c) and 2(d) in which the deformed GUV aspect ratio (i.e., the ratio of the major to minor axis) is $\epsilon = 1.33$.

## III. THEORY

### A. Acoustic scattering

Consider that the microvesicle center is at a distance $z_0$ from a pressure antinode. The incident pressure is distributed along the $z$ axis as

$$p_{in} = A\ \cos[k(z + z_0)] \cos \omega t, \tag{1}$$

where $A$ is the pressure amplitude, $k = \omega/c_0$ is the wave number, and $z_0$ is the distance of the microvesicle to an antinode at the origin of the coordinate system. It is convenient to adopt spherical coordinates $(r, \theta, \varphi)$. Because the microvesicles are much smaller than the wavelength, only the monopole and dipole modes are necessary to describe scattering. Thus the ratio of the microvesicle radius to the wavelength is limited to $a/\lambda < 0.1$ given our device operating wavelength $\lambda = 220\ \mu$m; this restricts us to $a < 22\ \mu$m. Moreover, as $h/a \ll 1$, we expect the acoustic scattering behavior of the microvesicle to be dominated by its liquid core [29]. Expanding the incident ($p_{in}$), transmitted ($p_{tr}$), and scattered pressures ($p_{sc}$)

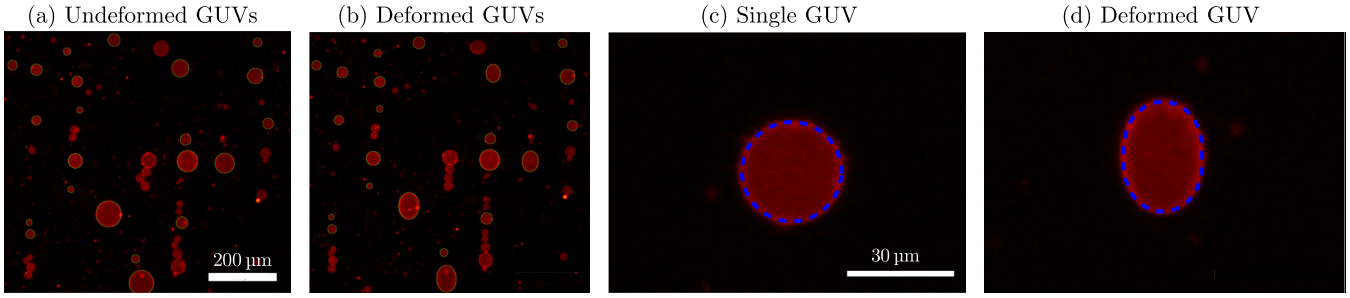


FIG. 2. Micrograph of GUVs in the one-dimensional acoustic field generated by the device operating with 6.7 MHz at room temperature. (a) GUVs are trapped by the acoustic radiation force. (b) Several GUVs from (a) are deformed. (c) A single trapped GUV of radius $a = 15.5\ \mu$m without deformation. (d) The GUV from (b) is deformed, with aspect ratio $\epsilon = 1.33$ and device voltage $V_{\rm pp} = 10$ V. The blue-dashed contour of the deformed GUV is obtained with Eq. (23).

yields [30]

$$\begin{bmatrix} p_{\rm in} \\ p_{\rm sc} \\ p_{\rm tr} \end{bmatrix} = A \sum_{n=0}^{1} (2n+1) \cos\left(\frac{n\pi}{2} + kz_0\right) \begin{bmatrix} j_n(kr) \\ s_n h_n^{(1)}(kr) \\ t_n j_n(c_0 kr/c_1) \end{bmatrix} \times P_n(\cos\theta), \tag{2}$$

where $j_n$ and $h_n^{(1)}$ are the spherical Bessel and Hankel (first-type) functions, $P_n$ is the $n$th-order Legendre polynomial, and $s_n$ and $t_n$ are the scattering and transmission coefficients which are calculated later. The term $\cos\omega t$ was omitted for simplicity. The core and surrounding liquid are assumed to behave as an ideal fluid.

Thermoviscous effects occur within the viscous $\delta_{\rm v}$ and thermal $\delta_{\rm th}$ boundary layers near the microvesicle's membrane. The boundary layers scale with frequency as $\omega^{-1/2}$. At the device's operational frequency 6.7 MHz in water at room temperature, we have [31] $\delta_{\rm v} = 0.19\ \mu$m and $\delta_{\rm th} = 0.081\ \mu$m. Given the small boundary layer thicknesses, we neglect these effects and consider only microvesicles with a diameter larger than 10 $\mu$m.

Acoustic streaming surrounding a microvesicle can disturb trapping stability and also deform the microvesicle membrane. To estimate this effect, we note that the trapping of a polystyrene particle with a diameter larger than 0.8 $\mu$m at 6.7 MHz is dominated by the acoustic radiation force [32]. In Fig. 2, we observe trapped microvesicles with a diameter above 10 $\mu$m; we thus assume that the GUV trapping stability is not disturbed by streaming. On the other hand, the deformation by acoustic streaming can be estimated by considering the stress induced on a rigid spherical particle by an incompressible fluid flow. The magnitude of this stress is given by [33] $\sigma_{\rm flow} = 3\eta v_{\rm s}/2a$, where $\eta$ is the dynamic viscosity of the fluid and $v_{\rm s}$ is the streaming velocity. The measured amplitude of acoustic streaming velocity induced in a microfluidic channel at 3.9 MHz is about [32] $v_{\rm s} = 0.05\ \mu{\rm m\,s^{-1}}$. Considering $a = 10\ \mu$m and $\eta = 8.9 \times 10^{-4}$ Pa s (water), we have $\sigma_{\rm flow} \sim 10^{-2}$ mPa. This is two orders of magnitude below the acoustic deformation stress. Therefore, the effects of acoustic streaming are not considered in our model.

Applying the continuity condition for the pressure and fluid velocity on the microvesicle membrane, we obtain the scattering and transmission coefficients as

$$s_n = \frac{\rho_0 c_0 j_n(ka) j_n'(c_0 ka/c_1) - \rho_1 c_1 j_n(c_0 ka/c_1) j_n'(ka)}{\rho_0 c_0 h_n^{(1)}(ka) j_n'(c_0 ka/c_1) - \rho_1 c_1 h_n^{(1)\prime}(ka) j_n(c_0 ka/c_1)}, \tag{3a}$$

$$t_n = \frac{\rho_1 c_1 [h_n^{(1)}(ka) j_n'(ka) - h_n^{(1)\prime}(ka) j_n(ka)]}{\rho_0 c_0 h_n^{(1)}(ka) j_n'(c_0 ka/c_1) - \rho_1 c_1 h_n^{(1)\prime}(ka) j_n(c_0 ka/c_1)}, \tag{3b}$$

where the prime symbol means differentiation with respect to the function argument.

### B. Acoustic radiation force and stress

The microvesicle will be trapped due to the action of the acoustic radiation force [34]

$$F_{\rm rad} = 4\pi a^2 k a E_0 \Phi \sin 2kz_0, \tag{4}$$

where $E_0 = \beta_0 A^2/4$ is the acoustic energy density. The entrapment occurs in a pressure node (antinode) with $kz_0 = \pi/2$ ($kz_0 = 0$), if the acoustophoretic contrast factor

$$\Phi = \frac{1}{3}\left(\frac{5\tilde{\rho}_1 - 2}{2\tilde{\rho}_1 + 1} - \tilde{\beta}_1\right) \tag{5}$$

is positive (negative), with $\tilde{\beta}_1 = \beta_1/\beta_0$ and $\tilde{\rho}_1 = \rho_1/\rho_0$. Using the parameters in Table I, we find that the GUVs will be trapped in nodes as $\Phi = 6.6 \times 10^{-3}$.

For an ideal fluid, the tangential components of the acoustic radiation stress vanish [35]: $\sigma_{r\theta} = \sigma_{r\varphi} = 0$. The radiation traction vector across the microvesicle's membrane is

TABLE I. Physical parameters of GUVs in an isotonic glucose solution at room temperature and pressure.

| Description | Value |
|---|---|
| Undeformed radius ($a$) | 6–20 $\mu$m |
| Density ratio ($\tilde{\rho}_1$) | 1.02 |
| Compressibility ratio ($\tilde{\beta}_1$) | 1.0 |
| Poisson's ratio ($\nu$) | 0.499 |
| Membrane thickness ($h$) | 2 nm |

expressed by

$$\delta \boldsymbol{t}_r = \left(\sigma_{rr}^{(0)}\big|_{r=a} - \sigma_{rr}^{(1)}\big|_{r=a}\right)\boldsymbol{e}_r, \tag{6}$$

where $\boldsymbol{e}_r$ is the radial unit vector and $\sigma_{rr}^{(1)}$ and $\sigma_{rr}^{(0)}$ are the radial components of the inner and outer acoustic radiation stress of the microvesicle—see Fig. 1. The radial stress is given by [36]

$$\sigma_{rr}^{(i)} = \frac{1}{4}(\rho_i|\boldsymbol{v}^{(i)}|^2 - \beta_i|p^{(i)}|^2) - \frac{\rho_i}{2}\left|v_r^{(i)}\right|^2, \quad i = 0, 1, \tag{7}$$

where $p^{(i)}$ is pressure and $\boldsymbol{v}^{(i)} = (i\rho_i\omega)^{-1}\nabla p^{(i)}$ is the fluid velocity vector, with $v_r^{(i)}$ being its radial component. The acoustic fields outside and inside the microvesicle are, respectively, $p^{(0)} = p_{\rm in} + p_{\rm sc}$ and $\boldsymbol{v}^{(0)} = \boldsymbol{v}_{\rm in} + \boldsymbol{v}_{\rm sc}$, $p^{(1)} = p_{\rm tr}$ and $\boldsymbol{v}^{(1)} = \boldsymbol{v}_{\rm tr}$. The radiation traction $\delta \boldsymbol{t}_r$ in a pressure node is obtained by substituting the pressure expressions given in (2) into Eq. (7)—see Appendix A. Accordingly, we have

$$\delta \boldsymbol{t}_r = \frac{9E_0(\tilde{\rho}_1 - 1)}{(2\tilde{\rho}_1 + 1)^2}[\tilde{\rho}_1 - (\tilde{\rho}_1 - 1)\cos^2\theta]\boldsymbol{e}_r. \tag{8}$$

The radiation traction does not depend on the microvesicle radius but on its density contrast. It also varies linearly with the acoustic energy density.

### C. Thin-shell deformation model

We assume that the microvesicle's membrane behaves as a thin elastic shell described by Young's modulus $E$ and Poisson's ratio $\nu$. The shell thickness $h$ is much smaller than the microvesicle's radius, $h \ll a$. We also assume that the internal fluid has an ambient pressure, which will be determined from its incompressibility. We chose the thin-shell elastic model because it accurately and straightforwardly describes the shape of a deformed vesicle subjected to external stresses [37,38]. In this approximation, the bending energy $U_{\rm b}$ is much smaller than the stretching energy $U_{\rm m}$ [39, p. 51], $U_{\rm b}/U_{\rm m} = O[(h/a)^2]$. We therefore neglect bending stresses in our analysis. On the other hand, bending energy is used in a deformation model which considers the membrane as a surface (with zero thickness) under external stresses [40]. In this case, the model descriptive parameter is the bending rigidity. The connection between the obtained results with the thin-shell and bending energy model is yet to be established.

The deformation traction (stress) across the membrane is given by

$$\delta \boldsymbol{t}_{\rm d} = \delta \boldsymbol{t}_r - \delta p\, \boldsymbol{e}_r, \tag{9}$$

where $\delta p = p_0 - p_1$ is the ambient pressure difference that will be determined later. The radiation stress causes a mechanical stress $\boldsymbol{\sigma}$ within the membrane. In the absence of volume forces, the induced stress (steady state) inside the thin elastic shell (membrane) obeys the equilibrium equation

$$\nabla \cdot \boldsymbol{\sigma} = \boldsymbol{0}, \tag{10}$$

with boundary conditions set by the inner and outer stresses to the microvesicle

$$\sigma_{rr}(a - h, \theta) = \sigma_{rr}^{(1)} - p_1, \tag{11a}$$

$$\sigma_{rr}(a, \theta) = \sigma_{rr}^{(0)} - p_0, \tag{11b}$$

$$\sigma_{r\theta}(a - h, \theta) = \sigma_{r\theta}(a, \theta) = 0. \tag{11c}$$

Stresses change a membrane point position at $\boldsymbol{R}(\theta') = a\boldsymbol{e}_r$ to $\boldsymbol{R}(\theta)$ through a small radial $u_r(\theta')\boldsymbol{e}_r$ and tangential $u_\theta(\theta')\boldsymbol{e}_\theta$ displacement. We thus write the membrane radius as $\boldsymbol{R}(\theta) = [a + u_r(\theta')]\boldsymbol{e}_r + u_\theta(\theta')\boldsymbol{e}_\theta$. The deformation geometry is then described by

$$R(\theta) = \sqrt{[a + u_r(\theta')]^2 + u_\theta^2(\theta')}. \tag{12}$$

The corresponding angular variation is $\Delta\theta' = \theta - \theta'$, with $\tan\Delta\theta' = u_\theta(\theta')/[a + u_r(\theta')]$. For a small angular change ($\Delta\theta' \ll 1$), we have $\Delta\theta' = u_\theta(\theta')/a + O[u_r(\theta')u_\theta(\theta')/a^2]$. Substituting this angle into Eq. (12) and Taylor expanding the result around $u_\theta/a, u_r/a = 0$ yields

$$R(\theta) = a + u_r(\theta) + O\left(u_\theta^2/a\right). \tag{13}$$

In the first-order approximation, tangential displacement $u_\theta$ can be neglected.

The radial displacement $u_r$ is calculated in Appendix B by solving Eq. (10) with the deformation boundary conditions using the Papikovich-Neuber method [41]. The result is

$$u_r(\theta) = \frac{a^2}{2Eh}\left[(1 - \nu)\left(\frac{3E_0(\tilde{\rho}_1 - 1)}{2\tilde{\rho}_1 + 1} - \delta p\right) - (5 + \nu)\frac{3E_0(\tilde{\rho}_1 - 1)^2}{(2\tilde{\rho}_1 + 1)^2}P_2(\cos\theta)\right]. \tag{14}$$

We note here that, with the thin-shell model, we recovered the radial displacement induced by an optical stretcher as reported in Ref. [37, Eq. 13a].

With the radius $R(\theta)$, we determine the ambient pressure difference $\delta p$ from the incompressibility condition of the microvesicle liquid core. We assume that this condition holds for the deformation time scale (in seconds), which is much larger than the acoustic time scale (in microseconds). Accordingly, the volume of the undeformed and deformed states are equal,

$$2\pi\int_0^{\pi/2} R^3(\theta)\cos^3\theta\, d\theta = \frac{4\pi a^3}{3}. \tag{15}$$

After expanding Eq. (14) around $\tilde{\rho}_1 = 1$ (mild density contrast) up to linear approximation, we obtain

$$u_r(\theta) = -\frac{a^2(1 - \nu)\delta p}{2Eh} + \frac{a^2E_0(1 - \nu)}{2Eh}(\tilde{\rho}_1 - 1) + O[(\tilde{\rho}_1 - 1)^2]. \tag{16}$$

Substituting this result into Eq. (15) yields

$$2Eh + a(1 - \nu)[\delta p - E_0(\tilde{\rho}_1 - 1)] = 2Eh, \tag{17}$$

whose solution is

$$\delta p = E_0(\tilde{\rho}_1 - 1). \tag{18}$$

Inserting this result into Eq. (14) gives

$$u_r(\theta) = -\frac{a^2E_0(\tilde{\rho}_1 - 1)^2}{Eh(2\tilde{\rho}_1 + 1)}\left[(1 - \nu) + \frac{3(5 + \nu)}{2(2\tilde{\rho}_1 + 1)}P_2(\cos\theta)\right]. \tag{19}$$

Using this approximated result in the integral of Eq. (15), we find the deformed microvesicle's volume to be $4\pi a^3/3 + O[(\tilde{\rho}_1 - 1)^2]$.

We notice that the ambient pressure difference acts to compress the microvesicle given that $\delta p > 0$. After substituting $\delta p$ into Eq. (B5) and considering the mild density contrast approach, we obtain the deformation traction as

$$\delta \boldsymbol{t}_{\mathrm{d}} = -\sigma_0[1 + P_2(\cos\theta)]\boldsymbol{e}_r, \tag{20}$$

where

$$\sigma_0 = \frac{2}{3}E_0(\tilde{\rho}_1 - 1)^2. \tag{21}$$

The peak radiation stress in Eq. (6) corresponds to

$$\sigma_{\mathrm{rad}} = \frac{9E_0\tilde{\rho}_1(\tilde{\rho} - 1)}{(1 + 2\tilde{\rho}_1)^2}. \tag{22}$$

The traction $\delta \boldsymbol{t}_{\mathrm{d}}$ tends to compress the microvesicle. The weakest stress occurs at $\theta = \pi/2$, $\sigma_{\min} = \sigma_0/2$, while the maximum stress is at $\theta = 0$, $\sigma_{\max} = 4\sigma_{\min}$.

We proceed to derive the microvesicle deformed geometry by substituting $\delta p$ into Eq. (12),

$$R(\theta) = a + \frac{a^2E_0(\tilde{\rho}_1 - 1)^2}{4Eh}\left[\frac{1 + 5\nu}{3} - (5 + \nu)\cos^2\theta\right]. \tag{23}$$

The aspect ratio of a deformed microvesicle is given by $\epsilon = R(\pi/2)/R(0)$. For a low density contrast, we Taylor expand the aspect ratio around $\tilde{\rho}_1 = 1$ as

$$\epsilon = 1 + \frac{aE_0}{4Eh}(5 + \nu)(\tilde{\rho}_1 - 1)^2. \tag{24}$$

We note that the aspect ratio does not depend on the wave frequency and is inversely proportional to the product of the membrane thickness and Young's modulus.

### D. Effects of other forces

When two microvesicles of radii $a$ in a pressure node are very close to each other, the secondary radiation force effects (interaction forces) may take place [42,43]. In this case, the magnitude of the interaction force is [42] $|\boldsymbol{F}_{\mathrm{int}}| \approx \pi a^2(2\sigma_0/3)(a/d)^4$, where $d$ is the interparticle distance. The corresponding average interaction stress is $\sigma_{\mathrm{int}} \approx (2\sigma_0/3)(a/d)^4$. The minimum interparticle distance is $d = 2a$, which implies that the largest interaction stress is given by $\sigma_{\mathrm{int}} \approx \sigma_0/24$. Therefore, comparing this stress with the smallest stress caused by the standing wave yields $\sigma_{\mathrm{int}}/\sigma_{\min} < 1/12$. We thus neglect stresses due to the secondary interaction forces in our analysis. However, when two microvesicles are very close (few nanometers apart), contact stresses, electrostatic forces between charged surfaces, and van der Waals forces between molecules may become prominent and are likely to induce additional deformation on the microvesicles. Hence we do not analyze the deformation of microvesicles within a 1 $\mu$m range of one another.

The fact that microvesicles sediment at the device's bottom requires an analysis of the influence of gravity on the acoustic deformation. The averaged stress due to gravity equals the vesicle's mass divided by its cross-section area, which leads to $\sigma_{\mathrm{gra}} = ag(\rho_1 - \rho_0)/2$, with $g = 9.8\ \mathrm{m\,s^{-2}}$ being acceleration due to gravity. From Table I, we consider $\rho_1 - \rho_0 = 20\ \mathrm{kg\,m^{-3}}$. Hence, for a GUV with a typical radius $a = 10\ \mu$m, we have $\sigma_{\mathrm{gra}} = 0.65$ mPa. We shall show in Sec. IV that the peak radiation stress is nearly 50 times stronger than this gravity stress. It follows that gravity deformation should be also about 1/50th of that caused by radiation stress. Therefore, we can neglect gravity force effects.

## IV. EXPERIMENTAL RESULTS

From acoustic pressure measurements performed with a fiber-optic hydrophone (Precision Acoustics, Dorset, UK), we measured the acoustic energy density for an excitation voltage of $10\ \mathrm{V_{pp}}$ to be $E_0 = (1.55 \pm 0.36)\ \mathrm{J\,m^{-3}}$. From Eq. (22) this corresponds to a peak radiation stress of $\sigma_{\mathrm{rad}} = (31 \pm 7.2)$ mPa, which suffices to produce observable deformations on the GUVs. Using Eq. (24), we can estimate the membrane Young's modulus of the GUV shown in Figs. 2(c) and 2(d) given that its radius and aspect ratio are $a = 15.5\ \mu$m and $\epsilon = 1.33$, respectively. Using the data shown in Table I, we obtain the membrane Young's modulus $E = 20.07$ Pa delivered power to the GUV of $P = 1\ \mu$W.

In Fig. 3(a), we show the aspect ratio of deformed GUVs versus undeformed radius $a$. We restrict our analysis to the isolated microvesicles with size ranging $5\ \mu\mathrm{m} < a < 16\ \mu\mathrm{m}$. Each point in the graph corresponds to the observation of 10 selected GUVs in a micrograph. The undeformed radii (before the acoustic field is active) are measured manually and have a 3% measurement variation (horizontal error bars). After setting the voltage to 10 V, the same selected GUVs are deformed within a few seconds (see Supplemental Material [28]). The aspect ratios of deformed GUVs were then measured manually from the micrographs. They have a variation as large as 22% (vertical error bars), which is compatible with the measurement uncertainty of 23% in the acoustic energy density. We note that the linear variation of the aspect ratio $\epsilon \sim a$ is predicted in Eq. (24) (solid line) and is in good agreement with the experimental data. The membrane Young's modulus of GUVs is estimated using the Levenberg-Marquardt (LM) algorithm with Eq. (24) as the fitting function. This algorithm solves the nonlinear least squares problem that appears in the curve fitting. The result gives $E = (23.88 \pm 2.81)$ Pa, which is similar to that measured from a single GUV shown in Fig. 2(d).

Figure 3(b) shows the aspect ratio as a function of the peak-to-peak voltage (squared) applied to the piezoelectric transducers. We assume that the acoustic energy density is proportional to the voltage squared, i.e., $E_0 = a_0V_{\mathrm{pp}}^2$, with $a_0 = 0.0155\ \mathrm{J\,m^{-3}\,V^{-2}}$. The protocol used to measure the aspect ratio is the same as described for Fig. 3(a). The obtained Young's modulus $E = (23.56 \pm 2.61)$ Pa is close to the estimated value from the data in Fig. 3(a). The linear variation of the aspect ratio $\epsilon \sim E_0$ (solid line) is noted. A measurement uncertainty of 22% (vertical error bar) is also observed in the data.

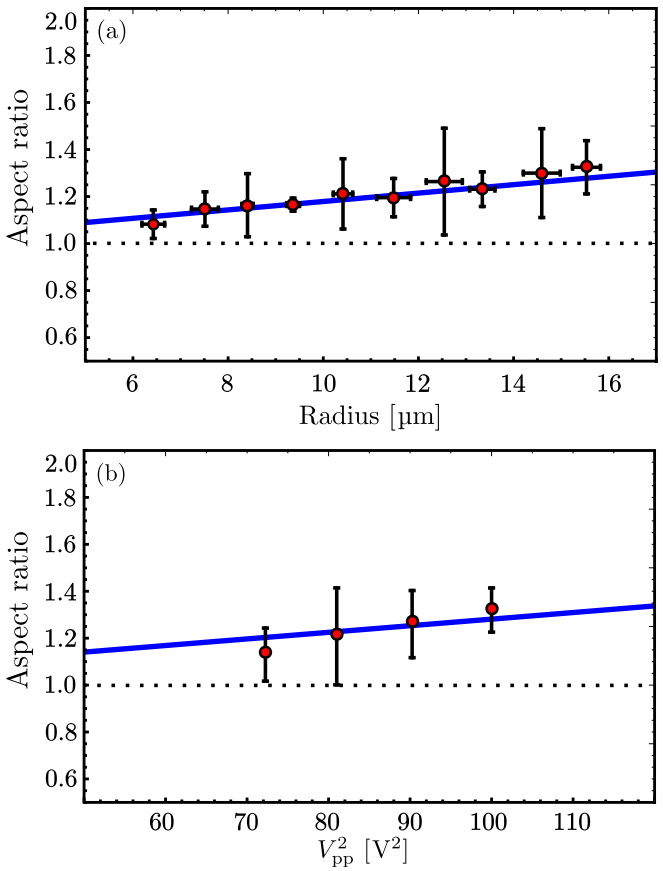


FIG. 3. Aspect ratio of deformed GUVs in the acoustic device operating at 6.7 MHz as a function of (a) radius $a$ with $V_{pp} = 10$ V, and (b) peak-to-peak applied voltage squared $V_{pp}^2$ with $a = 15.5$ $\mu$m. The horizontal and vertical bars are the error of measuring the undeformed radii and aspect ratios, respectively.

## V. DISCUSSION AND CONCLUSION

We have theoretically analyzed the acoustic deformation of soft lipid microvesicles (giant unilamellar vesicles—GUVs). We have assumed that the initial shape of a microvesicle is spherical. The model can be extended to spheroidal microvesicles using the formalism developed for the radiation force problem on spheroids as presented in Ref. [44]. A device comprised of two opposed piezoelectric transducers forming a square chamber produces a standing wave that can acoustically deform thousands of microvesicles simultaneously. To be deformed in this device, a microvesicle has to be trapped in a pressure node, although ultrasound absorption by the microvesicle may change the acoustic deformation stress [45]. The aspect ratio varies linearly with the microvesicle radius and the acoustic energy density inside the device's chamber $\epsilon \sim aE_0$. It also depends quadratically on the density contrast $\epsilon \sim (\tilde{\rho}_1 - 1)^2$. We note that deformation inversely scales with the membrane's thickness and Young's modulus, $\epsilon \sim (Eh)^{-1}$. The acoustic deformation does not depend on the device's operational frequency if the pressure amplitude is frequency independent.

In a set of experiments, we have confirmed the theoretical predictions for acoustic deformation. By analyzing the deformation as a function of microvesicle radius, we found the membrane Young's modulus of a population of GUVs to be $E = (23.88 \pm 2.81)$ Pa. Similarly, by varying the applied voltage to the piezoelectric transducers, we estimated $E = (23.56 \pm 2.61)$ Pa. GUV membrane stiffness is known to depend on the manufacturing process, e.g., Brochu and Vermette [46] reporting values in the 100s of pascals, albeit for much thicker GUV membrane structures. For comparison with biological specimens, myeloid and lymphoid soft cells have membrane Young's modulus in the range 100–200 Pa [47].

We also use our model to obtain the membrane Young's modulus of sRBC and green algae cell which were previously reported. By applying the LM algorithm to fit the aspect ratio data presented in Ref. [20, Fig. 5] with Eq. (24), we find the Young's modulus of a sRBC to be $E = 679$ Pa. This value is compatible with the Young's modulus of a sRBC reported in Ref. [20], $E = 629$ Pa. Similarly, we fit the aspect ratio data shown in Ref. [21, Fig. 17] to find the Young's modulus of a green algae as $E = 646$ Pa, which is consistent with the reported value $E = 687$ Pa.

Considering the typical range of acoustic energy density as [34] 1–100 J m$^{-3}$ and the density ratio of a sRBC being $\tilde{\rho}_1 = 1.1$, we see that the peak radiation stress $\sigma_{rad}$ is in the range 0.1–10 Pa. There is a similar deformation stress capability reported for optical stretchers [6], i.e., 1.02 Pa exerted on a sRBC with $a = 3.2$ $\mu$m and delivered power of 172 $\mu$W. The acoustic energy density and power per particle needed to generate the same optical stress on a sRBC is $E_0 = 51$ J m$^{-3}$ and $P = 4\pi a^2 c_0 E_0 = 9.84$ $\mu$W, respectively. Hence, the power required by acoustic deformation is four orders of magnitude smaller than for optical stretchers. The power produced within the device chamber is $P = A_{dev} c_0 E_0 = 3$ $\mu$W, where $A_{dev} = 40$ mm$^2$ is the device cross-section area.

Finally, acoustic deformation is a contactless method to assess the mechanical properties of lipid vesicles that covers the same stress range of optical stretchers but requires much less power. It can potentially be used to estimate the elasticity of thousands of cells within minutes. We believe that our method and analysis is a key first step towards the development of a versatile cell mechanophenotyping technique with unprecedented simplicity and high throughput.

## ACKNOWLEDGMENTS

G.T.S. and B.W.D. thank the Royal Society, UK (Newton Fund, Grant No. NA160200) and National Council for Scientific and Technological Development–CNPq, Brazil (Grant No. 307221/2016-4) for financial support. L.T. and S.M. thank BrisSynBio (BBSRC/EPSRC Synthetic Biology Research Centre, Grant No. BB/L01386X/1) at the University of Bristol for financial support. X.W. and X.H. thank the National Nature Science Foundation of China (Grant No. 21773050) for financial support.

G.T.S. and L.T. contributed equally to this work.

## APPENDIX A: ACOUSTIC RADIATION STRESS

To calculate the inner and outer radiation stresses of the microvesicle's membrane, we substitute the pressure fields given in (2) into Eq. (7) yielding

$$\sigma_{rr}^{(1)} = -E_0\tilde{\beta}_1|t_0|^2\left[j_0^2(c_0ka/c1) + [j_0'(c_0ka/c_1)]^2\right] \quad \text{(antinode)}, \tag{A1a}$$

$$\sigma_{rr}^{(0)} = -\frac{E_0}{2}\left[\frac{1}{2}\left|j_0(ka) + s_0h_0^{(1)}(ka)\right|^2 + \left|j_0'(ka) + s_0h_0^{(1)}(ka)\right|^2\right] \quad \text{(antinode)}, \tag{A1b}$$

$$\sigma_{rr}^{(1)} = \frac{9E_0}{(ka)^2\tilde{\rho}_1}|t_1|^2\left[j_1^2(c_0ka/c_1) - \frac{\cos^2\theta}{c_1^2}\left[\left(c_1^2 + c_0^2k^2a^2\right)j_1^2(c_oka/c_1) + (ka)^2c_0^2j_1'^2(c_0ka/c_1)\right]\right] \quad \text{(node)}, \tag{A1c}$$

$$\sigma_{rr}^{(0)} = \frac{9E_0}{(ka)^2}\left[\left|j_1(ka) + s_1h_1^{(1)}(ka)\right|^2 - \left[(1+k^2a^2)\left|j_1(ka) + s_1h_1^{(1)}(ka)\right|^2 + (ka)^2\left|j_1'(ka) + s_1h_1^{(1)'}(ka)\right|^2\right]\cos^2\theta\right] \quad \text{(node)}. \tag{A1d}$$

After inserting the coefficients given in (3) into (A1) and expanding the result around $ka = 0$ (Rayleigh scattering limit) with Mathematica Software (Wolfram Inc., USA), we find

$$\sigma_{rr}^{(1)} = -\tilde{\beta}_1E_0 + O[(ka)^2] \quad \text{(antinode)}, \tag{A2a}$$

$$\sigma_{rr}^{(0)} = -E_0 + O[(ka)^2] \quad \text{(antinode)}, \tag{A2b}$$

$$\sigma_{rr}^{(1)} = -\frac{9E_0\tilde{\rho}_1\cos 2\theta}{(2\tilde{\rho}_1+1)^2} + O[(ka)^2] \quad \text{(node)}, \tag{A2c}$$

$$\sigma_{rr}^{(0)} = -\frac{9E_0\left[1 - \tilde{\rho}_1^2 + \left(1+\tilde{\rho}_1^2\right)\cos 2\theta\right]}{2(2\tilde{\rho}_1+1)^2} + O[(ka)^2] \quad \text{(node)}. \tag{A2d}$$

Using this result in Eq. (6), we calculate the radiation traction at an antinode and node as, respectively,

$$\delta\boldsymbol{t}_r = E_0(\tilde{\beta}_1 - 1)\boldsymbol{e}_r + O[(ka)^2], \tag{A3a}$$

$$\delta\boldsymbol{t}_r = \frac{9E_0(\tilde{\rho}_1 - 1)}{(2\tilde{\rho}_1+1)^2}[\tilde{\rho}_1 - (\tilde{\rho}_1 - 1)\cos^2\theta]\boldsymbol{e}_r + O[(ka)^2]. \tag{A3b}$$

## APPENDIX B: DISPLACEMENT AND DEFORMATION STRESS

To solve Eq. (10), we use the Papkovich-Neuber method in which the radial displacement $u_r$ and the radial $\sigma_{rr}$ and meridional $\sigma_{r\theta}$ stresses inside the microvesicle membrane $a - h \leqslant r \leqslant a$ are given by [41]

$$u_r(\theta) = \sum_{n=0}^{\infty}\left[(n+1)(n-2+4\nu)a^{n+1}A_n + na^{n-1}B_n + n(n+3-4\nu)\frac{C_n}{a^n} - (n+1)\frac{D_n}{a^{n+2}}\right]P_n(\cos\theta), \tag{B1a}$$

$$\sigma_{rr}(r,\theta) = \frac{E}{1+\nu}\sum_{n=0}^{\infty}(n+1)\left[(n^2-n-2-2\nu)A_nr^n + \frac{n(n-1)}{n+1}B_nr^{n-2} - \frac{n(n^2+3n-2\nu)}{n+1}\frac{C_n}{r^{n+1}} + (n+2)\frac{D_n}{r^{n+3}}\right] \times P_n(\cos\theta), \tag{B1b}$$

$$\sigma_{r\theta}(r,\theta) = \frac{E}{1+\nu}\sum_{n=0}^{\infty}\left[(n^2-n-1+2\nu)r^nA_n + (n-1)r^{n-2}B_n + (n^2-2+2\nu)\frac{C_n}{r^{n+1}} - (n+2)\frac{D_n}{r^{n+3}}\right]\frac{dP_n(\cos\theta)}{d\theta}. \tag{B1c}$$

The unknown constants $A_n$, $B_n$, $C_n$, and $D_n$ are obtained from the boundary conditions which require the stress continuity across the inner $r = a - h$ and outer $r = a$ membrane surfaces.

After rewriting the radiation stresses in Eqs. (A2c) and (A2d) in terms of monopole ($n = 0$) and quadrupole ($n = 2$) modes, we obtain

$$\sigma_{rr}^{(i)} = \sigma_{rr}^{(i,0)} + \sigma_{rr}^{(i,2)}P_2(\cos\theta), \quad i = 0, 1, \tag{B2}$$

where

$$\sigma_{rr}^{(0,0)} = \frac{3E_0}{2\tilde{\rho}_1 + 1}, \quad \sigma_{rr}^{(0,2)} = -\frac{6E_0(\tilde{\rho}_1 - 1)}{(2\tilde{\rho}_1 + 1)^2}, \tag{B3a}$$

$$\sigma_{rr}^{(1,0)} = \frac{3E_0\tilde{\rho}_1}{2\tilde{\rho}_1 + 1}, \quad \sigma_{rr}^{(1,2)} = -\frac{6E_0\tilde{\rho}_1(\tilde{\rho}_1 - 1)}{(2\tilde{\rho}_1 + 1)^2}. \tag{B3b}$$

The boundary conditions described in (9) can be written as

$$\sigma_{rr}(a-h,\theta) = -p_1 + \sigma_{rr}^{(1,0)} + \sigma_{rr}^{(1,2)}P_2(\cos\theta), \tag{B4a}$$

$$\sigma_{rr}(a,\theta) = -p_0 + \sigma_{rr}^{(0,0)} + \sigma_{rr}^{(0,2)}P_2(\cos\theta), \tag{B4b}$$

$$\sigma_{r\theta}(a-h,\theta) = 0, \tag{B4c}$$

$$\sigma_{r\theta}(a,\theta) = 0. \tag{B4d}$$

Likewise, the deformation traction vector given in Eq. (6) can be written as

$$\delta\boldsymbol{t}_{\mathrm{d}} = \left[\delta t_{\mathrm{d}}^{(0)} + \delta t_{\mathrm{d}}^{(1)}P_2(\cos\theta)\right]\boldsymbol{e}_r, \tag{B5}$$

where

$$\delta t_{\mathrm{d}}^{(0)} = \frac{3E_0(\tilde{\rho}_1 - 1)}{2\tilde{\rho}_1 + 1} - \delta p, \tag{B6a}$$

$$\delta t_{\mathrm{d}}^{(2)} = -\frac{6E_0(\tilde{\rho}_1 - 1)^2}{(2\tilde{\rho}_1 + 1)^2}. \tag{B6b}$$

Combining Eqs. (B1b) and (B1c) with the boundary conditions in (B4), multiplying the result by $P_m(\cos\theta)$ and using the orthogonality relation of the Legendre polynomials $\int_{-1}^{1} P_m(x)P_n(x)dx = 2\delta_{mn}/(2n+1)$, we find the system of linear equations for the unknowns $A_0, A_2, B_2, C_2, D_0, D_2$ as

$$2E_0A_0 - \frac{2E_0}{(a-h)^3(1+\nu)}D_0 = p_1 - \sigma_{rr}^{(1,0)}, \tag{B7a}$$

$$2E_0A_0 - \frac{2E_0D_0}{a^3(1+\nu)} = p_0 - \sigma_{rr}^{(0,0)}, \tag{B7b}$$

$$\frac{6(a-h)^2\nu}{1+\nu}A_2 - \frac{2B_2}{1+\nu} - \frac{4(\nu-5)}{(a-h)^3(1+\nu)}C_2 - \frac{3}{(a-h)^5(1+\nu)}D_2 = \sigma_{rr}^{(1,2)}, \tag{B7c}$$

$$\frac{6a^2\nu}{1+\nu}A_2 - \frac{2B_2}{1+\nu} - \frac{4(\nu-5)}{a^3(1+\nu)}C_2 - \frac{3}{a^5(1+\nu)}D_2 = \sigma_{rr}^{(0,2)}, \tag{B7d}$$

$$\frac{(a-h)^2(7+2\nu)}{1+\nu}A_2 + \frac{B_2}{1+\nu} + \frac{2C_2}{(a-h)^3} - \frac{4D_2}{(a-h)^5(1+\nu)} = 0, \tag{B7e}$$

$$\frac{a^2(7+2\nu)}{1+\nu}A_2 + \frac{B_2}{1+\nu} + \frac{2C_2}{a^3} - \frac{4D_2}{a^5(1+\nu)} = 0. \tag{B7f}$$

These equations are solved with Mathematica Software (Wolfram Inc., USA) keeping only the leading terms of order $O[(h/a)^{-1}]$. Accordingly, we have

$$A_0 = -\frac{a}{6Eh}\delta t_{\mathrm{d}}^{(0)}, \tag{B8a}$$

$$A_2 = \frac{3-\nu}{70a(1-\nu)Eh}\delta t_{\mathrm{d}}^{(2)}, \tag{B8b}$$

$$B_2 = -\frac{a(2\nu^2+3\nu-11)}{30(1-\nu)Eh}\delta t_{\mathrm{d}}^{(2)}, \tag{B8c}$$

$$C_2 = \frac{a^4(2+\nu)}{30(1-\nu)Eh}\delta t_{\mathrm{d}}^{(2)}, \tag{B8d}$$

$$D_0 = -\frac{a^4(1+\nu)}{6Eh}\delta t_{\mathrm{d}}^{(0)}, \tag{B8e}$$

$$D_2 = -\frac{a^6(\nu^2+4\nu+7)}{140(1-\nu)Eh}\delta t_{\mathrm{d}}^{(2)}. \tag{B8f}$$

By replacing these coefficients in Eq. (B1a), and noting that all other coefficients of this equation are zero, we encounter the radial displacement as

$$u_r(\theta) = \frac{a^2}{4Eh}\left[2(1-\nu)\delta t_{\mathrm{d}}^{(0)} + (5+\nu)\delta t_{\mathrm{d}}^{(2)} P_2(\cos\theta)\right]. \tag{B9}$$

Replacing the equations in (B6) into this equation results in

$$u_r(\theta) = \frac{a^2}{2Eh}\left[(1-\nu)\left(\frac{3E_0(\tilde{\rho}_1-1)}{2\tilde{\rho}_1+1} - \delta p\right) - (5+\nu)\frac{3E_0(\tilde{\rho}_1-1)^2}{(2\tilde{\rho}_1+1)^2} P_2(\cos\theta)\right]. \tag{B10}$$


[1] J. Lin, D. Kim, H. T. Tse, P. Tseng, L. Peng, M. Dhar, S. Karumbayaram, and D. D. Carlo, Microsyst. Nanoeng. **3**, 17013 (2017).

[2] N. Toepfner, C. Herold, O. Otto, P. Rosendahl, A. Jacobi, M. Kräter, J. Stächele, L. Menschner, M. Herbig, L. Ciuffreda, L. Ranford-Cartwright, M. Grzybek, Ü. Coskun, E. Reithuber, G. Garriss, P. Mellroth, B. Henriques-Normark, N. Tregay, M. Suttorp, M. Bornhäuser, E. R. Chilvers, R. Berner, and J. Guck, eLife **7**, e29213 (2018).

[3] D. A. Fedosov, H. Lei, B. Caswell, S. Suresh, and G. E. Karniadakis, PLoS Comput. Biol. **7**, e1002270 (2011).

[4] C. Alibert, B. Goud, and J.-B. Manneville, Biol. Cell **109**, 167 (2017).

[5] R. M. Hochmuth, J. Biomech. **33**, 15 (2000).

[6] J. Guck, R. Ananthakrishnan, T. J. Moon, C. C. Cunningham, and J. Käs, Phys. Rev. Lett. **84**, 5451 (2000).

[7] M. Radmacher, Methods Cell Biol. **83**, 347 (2007).

[8] D. R. Gossett, H. T. K. Tse, S. A. Lee, Y. Ying, A. G. Lindgren, O. O. Yang, J. Rao, A. T. Clark, and D. D. Carlo, Proc. Natl. Acad. Sci. USA **109**, 7630 (2012).

[9] O. Otto, P. Rosendahl, A. Mietke, S. Golfier, C. Herold, D. Klaue, S. Girardo, S. Pagliara, A. Ekpenyong, A. Jacobi, M. Wobus, N. Topfner, U. F. Keyser, J. Mansfeld, E. Fischer-Friedrich, and J. Guck, Nat. Methods **12**, 199 (2015).

[10] G. T. Silva, J. Acoust. Soc. Am. **136**, 2405 (2014).

[11] G. T. Silva, A. L. Baggio, J. H. Lopes, and F. G. Mitri, IEEE Trans. Ultrason. Ferroelect. Freq. Control **62**, 576 (2015).

[12] L. Zhang, J. Acoust. Soc. Am. **144**, 443 (2018).

[13] H. Bruus, J. Dual, J. Hawkes, M. Hill, T. Laurell, J. Nilsson, S. Radel, S. Sadhal, and M. Wiklund, Lab. Chip **11**, 3579 (2011).

[14] M. Caleap and B. W. Drinkwater, Proc. Natl. Acad. Sci. USA **111**, 6226 (2014).

[15] D. J. Collins, B. Morahan, J. Garcia-Bustos, C. D. M. Plebanski, and A. Neild, Nat. Commun. **6**, 8686 (2015).

[16] L. Tian, N. Martin, P. G. Bassindale, A. J. Patil, M. Li, A. Barnes, B. W. Drinkwater, and S. Mann, Nat. Commun. **7**, 13068 (2016).

[17] P. Augustsson, J. T. Karlsen, H.-W. Su, H. Bruus, and J. Voldman, Nat. Commun. **7**, 11556 (2016).

[18] P. L. Marston and R. E. Apfel, J. Colloid Interface Sci. **68**, 280 (1979).

[19] P. L. Marston and R. E. Apfel, J. Acoust. Soc. Am. **67**, 27 (1980).

[20] P. Mishra, M. Hill, and P. Glynne-Jones, Biomicrofluidics **8**, 034109 (2014).

[21] F. B. Wijaya, A. R. Mohapatra, S. Sepehrirahnama, and K. Lim, Microfluid. Nanofluid. **20**, 69 (2016).

[22] J. Y. Hwang, J. Kim, J. M. Park, C. Lee, H. Jung, J. Lee, and K. K. Shung, Sci. Rep. **6**, 27238 (2016).

[23] P. Walde, K. Cosentino, H. Engel, and P. Stano, Chembiochem. **11**, 848 (2010).

[24] E. Schafer, T. T. Kliesch, and A. Janshoff, Langmuir **29**, 10463 (2013).

[25] E. Schafer, M. Vache, T. T. Kliesch, and A. Janshoff, Soft Matter **11**, 4487 (2015).

[26] L. Lu, W. J. Doak, J. W. Schertzer, and P. R. Chiarot, Soft Matter **12**, 7521 (2016).

[27] L. B.-A. Johansson, B. Kalman, G. Wikander, A. Fransson, K. Fontell, B. Bergenstahl, and G. Lindblom, Biochim. Biophys. Acta **1149**, 285 (1993).

[28] See Supplemental Material at http://link.aps.org/supplemental/10.1103/PhysRevE.99.063002 for further details on GUV preparation and acoustic measurements, which includes Refs. [48–50].

[29] J. P. Leão-Neto, J. H. Lopes, and G. T. Silva, Phys. Rev. Appl. **6**, 024025 (2016).

[30] T. Hasegawa, J. Acoust. Soc. Am. **65**, 32 (1979).

[31] J. T. Karlsen and H. Bruus, Phys. Rev. E **92**, 043010 (2015).

[32] R. Barnkob, P. Augustsson, T. Laurell, and H. Bruus, Phys. Rev. E **86**, 056307 (2012).

[33] H. Bruus, *Theoretical Microfluidics* (Oxford University Press, New York, 2008).

[34] H. Bruus, Lab Chip **12**, 1014 (2012).

[35] P. L. Marston, J. Acoust. Soc. Am. **67**, 15 (1980).

[36] C. P. Lee and T. G. Wang, J. Acoust. Soc. Am. **94**, 1099 (1993).

[37] J. Guck, R. Ananthakrishnan, H. Mahmood, T. J. Moon, C. C. Cunningham, and J. Käs, Biophys. J. **81**, 767 (2001).

[38] A. Mietke, O. Otto, S. Girardo, P. Rosendahl, A. Taubenberger, S. Golfier, E. Ulbricht, S. Aland, J. Guck, and E. Fischer-Friedrich, Biophys. J. **109**, 2023 (2015).

[39] L. D. Landau, L. P. Pitaevskii, A. M. Kosevich, and E. M. Lifshitz, *Theory of Elasticity* (Butterworth-Heinemann, London, 2012).

[40] U. Seifert, Eur. Phys. J. B **8**, 405 (1999).

[41] A. I. L'ure, *Three-dimensional Problems of the Theory of Elasticity* (John Wiley & Sons, Inc., New York, 1964).

[42] G. T. Silva and H. Bruus, Phys. Rev. E **90**, 063007 (2014).

[43] J. H. Lopes, M. Azarpeyvand, and G. T. Silva, IEEE Trans. Ultrason. Ferroelectr. Freq. Control **63**, 186 (2016).

[44] G. T. Silva and B. W. Drinkwater, J. Acoust. Soc. Am. **144**, EL453 (2018).
[45] J. P. Leão-Neto and G. T. Silva, Ultrasonics **71**, 1 (2016).
[46] H. Brochu and P. Vermette, Langmuir **24**, 2009 (2009).
[47] E. M. Darling and D. D. Carlo, Annu. Rev. Biomed. Eng. **17**, 35 (2015).
[48] C. Mauroy, T. Portet, M. Winterhalder, E. Bellard, M. C. Blache, J. Teissie, A. Zumbusch, and M. P. Rols, Bioelectrochemistry **87**, 253 (2012).
[49] H. M. Bi, B. Yang, L. Wang, W. W. Cao, and J. X. Han, J. Mater. Chem. A **1**, 7125 (2013).
[50] P. Morris, A. Hurrell, A. Shaw, E. Zhang, and P. Beard, J. Acoust. Soc. Am. **125**, 3611 (2009).